Chapter 4

Characterizing Super-flares in V711 Tau using Time-resolved Spectroscopy (TRS)

In this work, we analyze three energetic X-ray flares from the active RS CVn binary HR 1099 using data obtained from XMM-Newton. The flare duration ranges from 2.8 to 4.1 h, with e-folding rise and decay times in the range of 27 to 38 minutes and 1.3 to 2.4 h, respectively, indicating rapid rise and slower decay phases. The flare frequency for HR 1099 is one flare per rotation period. Time-resolved spectroscopy reveals peak flare temperatures of 39.44, 35.96, and 32.48 MK, emission measures of 7×10^{53} ***to*** 8×10^{54} ***cm***$^{-3}$***, global abundances of 0.250, 0.299, and 0.362*** $Z_{\odot}$***, and peak X-ray luminosities of*** $10^{31.21-32.29}$ ***erg s***$^{-1}$***. The quiescent state is modeled with a three-temperature plasma maintained at 3.02, 6.96, and 12.53 MK. The derived flare semi-loop lengths of 6 to 8.9*** $\times10^{10}$ ***cm were found to be comparable to the other flares detected on HR 1099; however, they are significantly larger than typical solar flare loops. The estimated flare energies, ranging from*** $10^{35.83-37.03}$ ***erg, classify these flares as superflares. The magnetic field strengths of the loops are found to be in the range of 350 to 450 G. We diagnose the physical***

conditions of the flaring corona in HR 1099 through the observations of superflares and provide an inference on the plasma processes.

4.1 HR 1099

HR 1099 (= V711 Tauri) is the RS CVn type binary (Bopp and Fekel, 1976) located in the Taurus constellation at a distance of 29.43 ± 0.03 pc (Gaia Collaboration, 2020). Comprising a pair of solar-type stars, HR 1099 is composed of a K1IV star as primary and a smaller, rapidly rotating G5V secondary. This system exhibits a short orbital period of approximately 2.82 days (Bopp and Fekel, 1976; Fekel, 1983), resulting in close proximity between these two stars. One of the key features that sets HR 1099 apart is its exceptional magnetic activity. Both stars in the system generate strong magnetic fields, which in turn give rise to various physical phenomena, including surface inhomogeneity, stellar flares, X-ray emissions, and other forms of high-energy radiations, including gamma and UV radiations (e.g. García-Alvarez et al., 2003; Osten et al., 2004). This makes HR 1099 an ideal target for studying the complex magnetic activities resulting from X-rays and other wavelengths.

HR 1099 has been extensively observed in the past from X-ray to radio wavelengths (e.g. Ayres et al., 2001; García-Alvarez et al., 2003; Osten et al., 2004; Strassmeier and Bartus, 2000). Many authors have done extensive analysis to identify magnetic activity cycles in HR 1099 using long-term photometry, a method known for its ability to detect changes in spot coverage. These investigations have yielded varying periods ranging from 14 – 20 yrs (Berdyugina and Henry, 2007; Lanza et al., 2006; Muneer et al., 2010). Perdelwitz et al. (2018) explored the long-term X-ray activity cycle and found no statistically significant periodic variations in the X-ray dataset. HR 1099 is prone to X-ray flaring events (e.g. Barthelmy, 2014; Kawai et al., 2017; Nordon and Behar, 2007; Pandey and Singh, 2012).

The loop geometry in the corona of HR 1099 has been studied in the past, reporting loop length of the order of 10^{10} cm (Mullan et al., 2006; Tsuboi et al., 2016).

This study delves into the X-ray flares on HR 1099, utilizing data obtained from the XMM-Newton satellite. By making a detailed study of XMM-Newton observations and its X-ray spectra and light curves, we studied three superflares and derived their physical properties, loop parameters, and abundance variations. The activity level of HR 1099 appears to have remained relatively stable over time, making this type of study valuable for enhancing our understanding of the star's physical properties. It also contributes to the long-term monitoring of superflares and provides insights into variations in their behavior.

4.2 Observation and Data Reduction

The log of observation of the two data sets A1 and A2, which are analyzed in this chapter, is given in Table 2.1, and the standard data reduction procedure applied to these data sets is discussed in Chapter 2. While doing so, we observed a significant pile-up in the dataset for observation of set A1, while no pile-up effect was detected in the case of set A2. However, both data sets were found to be free of proton flare events for energies exceeding 10 keV. To mitigate the observed pile-up effect, we opted for annulus regions with inner and outer radii of 15" and 55" for set A1, as mentioned in 2.1.

4.3 Analysis and Results

In this section, we focus on analyzing the temporal and spectral characteristics of the X-ray observations.

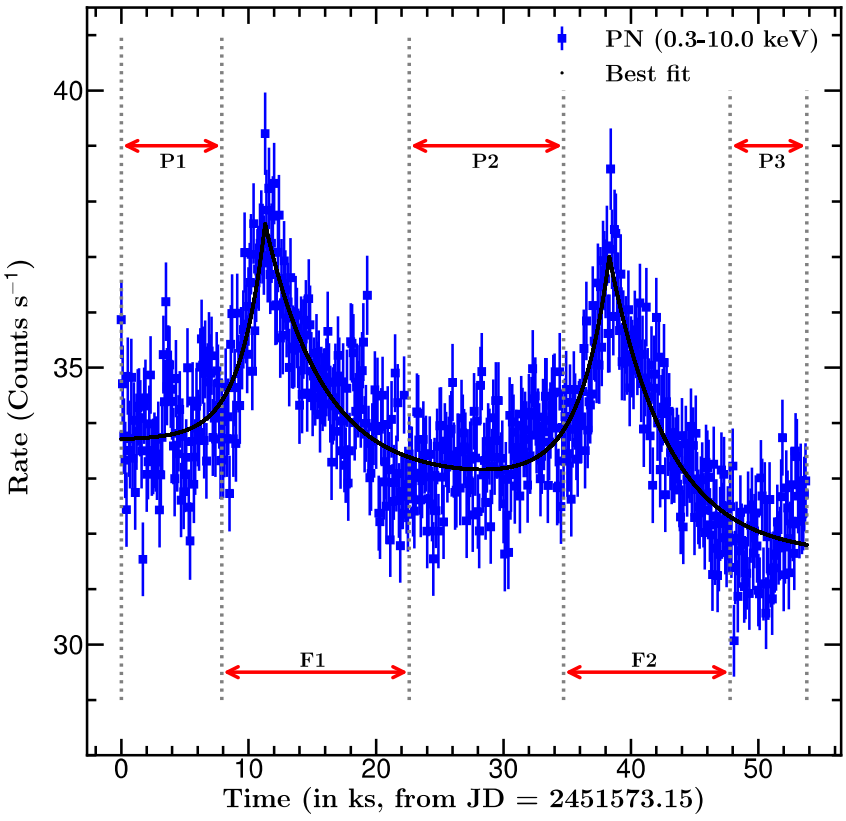

(a) A1

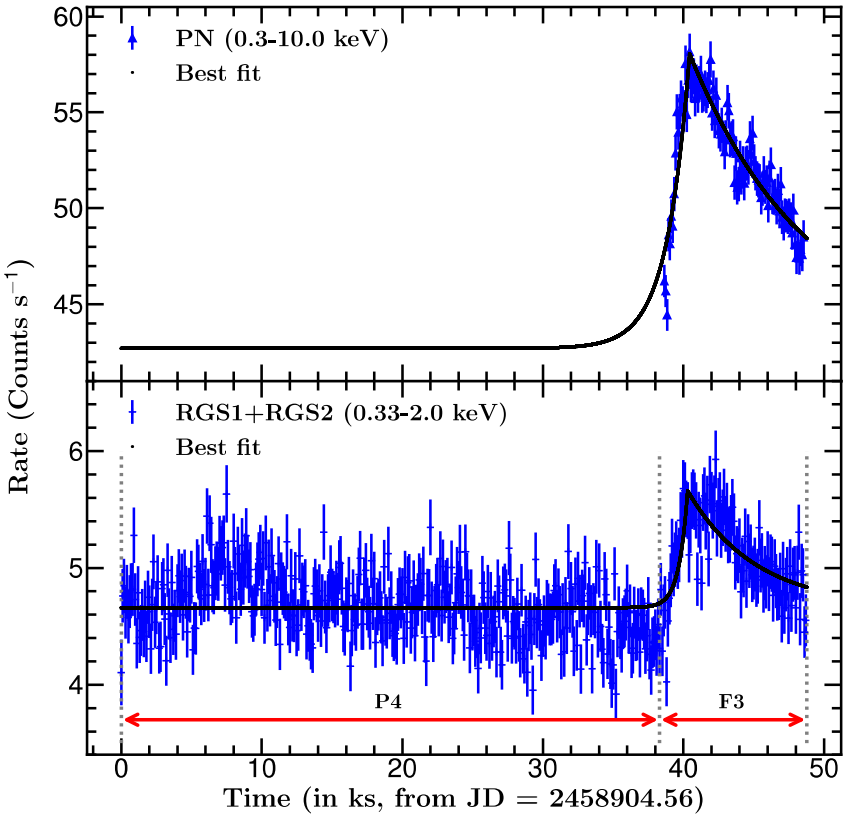

(b) A2

Figure 4.1: X-ray light curves of HR 1099 in different detectors. The flaring regions are marked by the vertical lines.

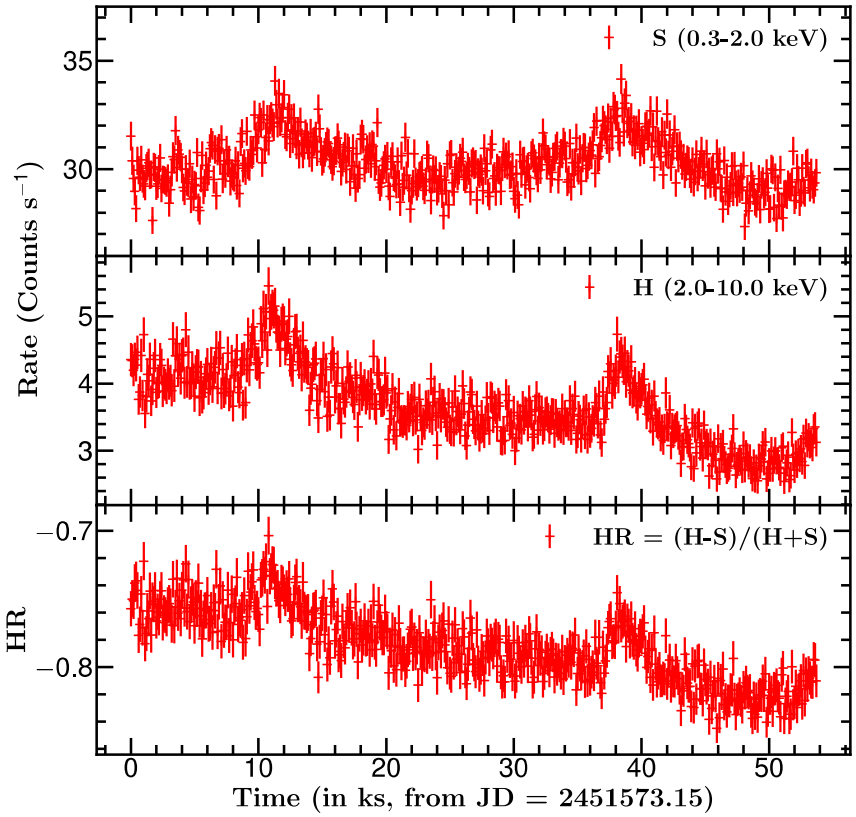

(a) A1

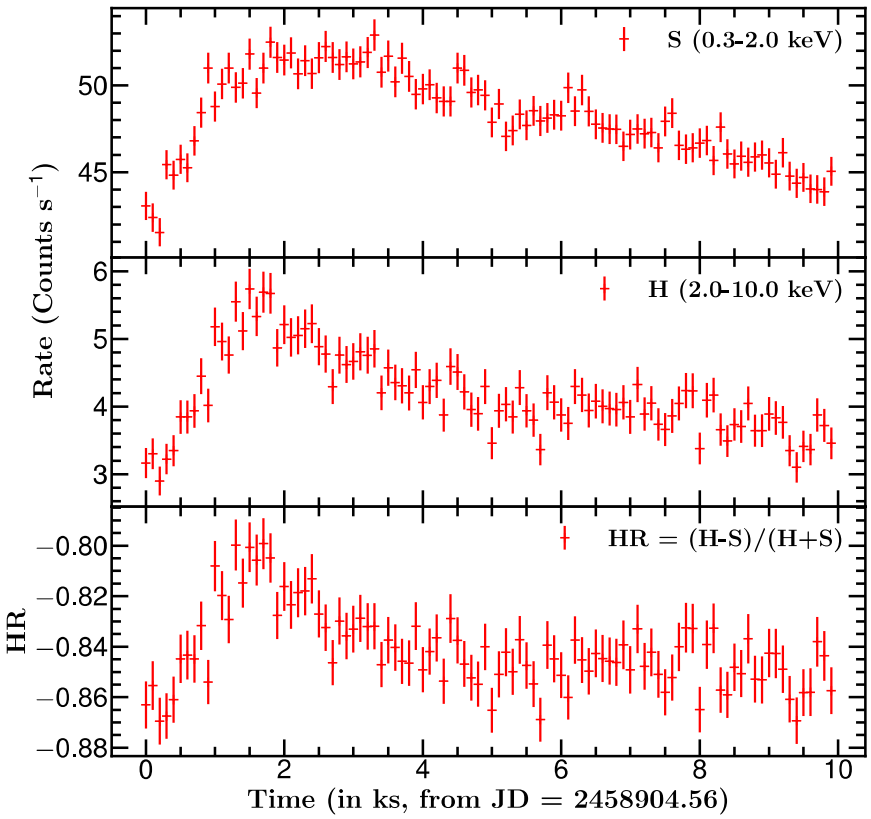

(b) A2

Figure 4.2: Soft and hard X-ray light curves along with the HR curve with 100s binning.

4.3.1 X-ray Light Curves

Fig. 4.1 represents the X-ray light curves with 100 s binning, obtained from PN and RGS detectors covering the energy range 0.3 - 10 keV and 0.33 - 2.0 keV, respectively. The temporal variability of counts exhibits flare-like features with a significant increase in the count rate observed during both observations. We identified a total of three flares, namely F1, F2, and F3. The pre- and post-flare time segments with nearly constant counts are referred to as P1 to P4, serving as proxies for quiescent states. All these regions are marked in Fig. 4.1. We also used the criteria to rule out the possibility of false flare detection using only flares with a duration longer than 5 min and having at least 5 consecutive data points exceeding 3 σ (Maehara et al., 2012, 2015). However, we were unable to analyze pixel-level data as described in Maehara et al. (2012) due to the broad Point Spread Function (PSF) of XMM-Newton, with a Full Width at Half Maximum (FWHM) of approximately 15 arcseconds for the MOS cameras and around 6.6 for the PN (Strüder et al., 2001; Turner et al., 2001). Thus, the CCDs are primarily aimed at spectral and temporal analysis rather than spatially precise, pixel-level variability studies. Additionally, as noted in Section 4.2, we confirmed the absence of high-energy background flares and other X-ray sources in the vicinity. The active K-type subgiant, being the primary X-ray emitter alongside a less active G-type main-sequence companion, rules out any flare contamination from other sources (Bopp and Fekel, 1976; Linsky et al., 1989).

Additionally, we have plotted the light curve in two energy bands, namely soft (S; 0.2-2.0 keV) and hard (H; 2.0-10.0 keV) energy bands, along with the hardness ratio (HR), defined as HR = (H-S)/(H+S), in Fig. 4.2. The HR curve closely follows the flaring events in the light curves, indicating the rise in temperature of the X-ray emitting region with an increase in HR during the flares. The HR increase confirms the coronal heating as well as it rules out the instrumental artifacts.

Table 4.1: The best-fit parameters for all the observed flares.

Parameters (→) Flare (↓)	τ_r (ks)	τ_d (ks)	A_P (counts s^{-1})	A_Q (counts s^{-1})
A1/F1 (PN)	2.0±0.2	4.5±0.2	39.2±0.7	33.7
A1/F2 (PN)	2.3±0.2	4.6±0.4	38.6±0.7	33.0
A2/F3 (RGS)	0.6±0.1	4.9±0.7	5.9±0.2	4.6
(PN)	1.6±0.1	8.5±0.4	58.2±0.9	42.7*

A_P and A_Q are the count rates of the flare peak and quiescent states, respectively.
* Quiescent state count rates were estimated from RGS1 order 1 with an average count rate during the P4 state of 1.57 count s^{-1} using the WebPIMMS[1].

Following equation 3.1 as mentioned in Chapter 3, we derived the rise and decay times for all three flares. The e-folding rise times for the flares were found to range from 1.6 to 2.3 ks, whereas the decay times ranged from 4.5 to 8.5 ks, indicating a rapid rise and slower decay pattern. Table 4.1 lists the rise and decay times obtained from the light curves, and Fig. 4.1 illustrates the modeled light curves. The peak flare count rates were increased by 16 to 36% of the quiescent state count rate in these flares.

4.3.2 EPIC Spectral Analysis

To monitor variations in X-ray spectral parameters across all observations, we performed X-ray spectral analysis of quiescent and flaring states separately on the PN data, as it provides a better signal-to-noise (S/N) ratio. The spectral analysis was performed with Astrophysical Plasma Emission Code (APEC; Smith et al., 2001) using XSPEC, version 12.12 (Arnaud, 1996). The detailed spectral analyses are described in forthcoming sections.

4.3.2.1 The quiescent state spectroscopy

For determining the quiescent temperature and emission measure, pre/post-flare segments with nearly constant counts, marked as P1 to P4, were considered as the proxy of the quiescent. For set A1, we modeled the segmented spectra from P1 to P3 using one temperature (1-T), two temperatures (2-T), three temperatures (3-T), and four-temperature

(4-T) plasma models APEC with varying parameters such as temperatures, corresponding normalization parameters, and abundances. Here, we used the TBABS absorption model for hydrogen column density (N_H) and fixed it to the maximum value of galactic N_H of 10^{18} cm^{-2} for HR 1099. We adopted solar abundances ($Z_\odot$) from Wilms et al. (2000). Abundances of all components were tied and varied together for the multi-component plasma model. The 3-T model fits the spectra well but gives varying temperatures for each P1, P2, and P3 segment. While adding one more component, the first three cool temperatures remained constant, whereas the fourth temperature varied for all the quiescent state segments. The average quiescent temperatures of cool components were found to be 0.26, 0.5, and 1.08 keV, with a weighted average temperature of 0.82 keV, calculated using equation 3.2.

For set A2, the PN data included only the flare part without the pre/post-flare segments throughout the observations. Therefore, we divided flare F3 into segments (rise, peak, and decay) with sufficient counts and applied the same procedure as applied for set A1. Again, the fourth temperature was found to be varying, while the first three temperatures remained nearly constant across all the segments. The coolest three temperatures were found to be similar to that for set A1 within one sigma level. Thus, for further analysis, the quiescent corona of HR 1099 was assumed to be best represented by a three-temperature plasma. All the derived spectral parameters for the quiescent states are given in Table 4.2.

4.3.2.2 Spectral evolution during the flares

We divided the flaring part of the light curve into distinct time intervals of rise, peak, and decay phases to understand the flare evolution. These phases are denoted as Ri, P, and Di, where the index 'i' can take values from 1 onwards. The duration of each flare segment was chosen to ensure an equal number of counts within each interval.

Table 4.2: Spectral parameters of the quiescent using 4-T APEC model for all the data sets, within a 68% confidence range.

Para	Set A1	Set A2
kT_1 (keV)	$0.26^{+0.03}_{-0.03}$	$0.26^{+0.02}_{-0.02}$
kT_2 (keV)	$0.5^{+0.1}_{-0.1}$	$0.59^{+0.09}_{-0.08}$
kT_3 (keV)	$1.08^{+0.03}_{-0.02}$	$1.07^{+0.04}_{-0.03}$
kT_4 (keV)	$2.3^{+0.1}_{-0.09}$	$2.6^{+0.2}_{-0.1}$
T_Q* (keV)	$0.82^{+0.06}_{-0.05}$	$0.8^{+0.1}_{-0.1}$
EM_1 ($10^{53} cm^{-3}$)	$1.4^{+0.4}_{-0.5}$	29^{+3}_{-4}
EM_2 ($10^{53} cm^{-3}$)	$0.8^{+0.5}_{-0.4}$	15^{+5}_{-4}
EM_3 ($10^{53} cm^{-3}$)	$3.9^{+0.4}_{-0.3}$	70^{+7}_{-7}
EM_4 ($10^{53} cm^{-3}$)	$5.9^{+0.3}_{-0.3}$	64^{+6}_{-6}
EM_Q* ($10^{53} cm^{-3}$)	$2.0^{+0.3}_{-0.2}$	38^{+3}_{-3}
Z ($Z_\odot$)	$0.26^{+0.03}_{-0.03}$	$0.34^{+0.03}_{-0.03}$
χ^2_ν (dof)	1.09 (566)	1.14 (502)

*For the calculation of T_Q and EM_Q, only the first three temperatures and emission measures have been used.

We applied a consistent approach for all flares analyzed here. Each segmented spectrum was modeled using a 4-T APEC model. The temperatures and emission measures of the first three plasma components were fixed at their corresponding quiescent values, allowing the parameters of the fourth component to vary in order to obtain the flare-specific parameters. The parameters derived for each flare are given in Table 4.3. The temporal variations of these parameters are illustrated in Fig. 4.3, demonstrating that nearly all parameters peak during the peak phase of the flare. The peak flare temperature, kT_4, was found to be 3.4, 3.1, and 2.8 keV, while the peak emission measure, EM_4, reached 7.1, 7.0, and $81 \times 10^{53} cm^{-3}$ for flares F1, F2, and F3, respectively. We determined the unabsorbed flux for each flare segment using the convolution model CFLUX and integrated this flux across all segments to obtain the total flux (F). From this, we derived the luminosity ($L_{XF} = 4\pi D^2 F$) and the total flare energy ($E_{X,Total} = L_{XF} \times (\tau_r + \tau_d)$), where D represents the distance to the object in cm. The resulting values for L_{XF} and $E_{X,Total}$ are presented in Table 4.4. The

Table 4.3: Best fit spectral parameters for each time segment during the flares F1 to F3 within 68% confidence interval.

Parameters (→) Flare (↓)	FS	kT_4 (keV)	EM_4 ($10^{53} cm^{-3}$)	Z ($Z_\odot$)	L_{XF} (10^{31} erg s^{-1})	χ^2_ν (dof)
F1	R1	$3.4^{+0.1}_{-0.1}$	$5.7^{+0.2}_{-0.2}$	$0.217^{+0.007}_{-0.007}$	$1.421^{+0.009}_{-0.009}$	1.12 (416)
	R2	$3.3^{+0.1}_{-0.1}$	$6.0^{+0.2}_{-0.2}$	$0.228^{+0.009}_{-0.009}$	$1.46^{+0.01}_{-0.01}$	1.08 (372)
	P	$3.4^{+0.1}_{-0.1}$	$7.1^{+0.2}_{-0.2}$	$0.233^{+0.009}_{-0.009}$	$1.62^{+0.01}_{-0.01}$	1.16 (395)
	D1	$3.32^{+0.1}_{-0.09}$	$6.9^{+0.2}_{-0.2}$	$0.250^{+0.009}_{-0.009}$	$1.60^{+0.01}_{-0.01}$	1.14 (386)
	D2	$3.29^{+0.09}_{-0.08}$	$6.5^{+0.2}_{-0.2}$	$0.246^{+0.009}_{-0.009}$	$1.53^{+0.01}_{-0.01}$	1.02 (388)
	D3	$3.0^{+0.1}_{-0.1}$	$6.2^{+0.2}_{-0.2}$	$0.238^{+0.009}_{-0.008}$	$1.47^{+0.01}_{-0.01}$	1.04 (377)
	D4	$2.9^{+0.1}_{-0.1}$	$6.0^{+0.2}_{-0.2}$	$0.24^{+0.01}_{-0.01}$	$1.45^{+0.01}_{-0.01}$	1.05 (346)
F2	R1	$2.51^{+0.09}_{-0.09}$	$6.0^{+0.2}_{-0.2}$	$0.267^{+0.009}_{-0.009}$	$1.43^{+0.01}_{-0.01}$	1.0 (371)
	R2	$2.57^{+0.09}_{-0.09}$	$6.3^{+0.2}_{-0.2}$	$0.281^{+0.009}_{-0.009}$	$1.49^{+0.01}_{-0.01}$	0.97 (375)
	P	$3.1^{+0.1}_{-0.1}$	$7.0^{+0.2}_{-0.2}$	$0.299^{+0.009}_{-0.009}$	$1.68^{+0.01}_{-0.01}$	1.05 (405)
	D1	$2.7^{+0.1}_{-0.1}$	$6.5^{+0.2}_{-0.2}$	$0.293^{+0.009}_{-0.01}$	$1.55^{+0.01}_{-0.01}$	1.08 (372)
	D2	$2.5^{+0.1}_{-0.1}$	$6.2^{+0.2}_{-0.2}$	$0.297^{+0.01}_{-0.009}$	$1.50^{+0.01}_{-0.01}$	0.96 (362)
	D3	$2.41^{+0.08}_{-0.08}$	$5.8^{+0.2}_{-0.2}$	$0.27^{+0.01}_{-0.01}$	$1.41^{+0.01}_{-0.01}$	1.04 (357)
	D4	$2.4^{+0.1}_{-0.1}$	$5.3^{+0.2}_{-0.2}$	$0.291^{+0.009}_{-0.009}$	$1.39^{+0.01}_{-0.01}$	1.15 (359)
	D5	$2.3^{+0.1}_{-0.1}$	$5.1^{+0.2}_{-0.2}$	$0.286^{+0.009}_{-0.009}$	$1.34^{+0.01}_{-0.01}$	0.93 (363)
F3	R	$2.64^{+0.08}_{-0.07}$	60^{+2}_{-1}	$0.331^{+0.006}_{-0.006}$	$16.83^{+0.01}_{-0.01}$	1.17 (489)
	P	$2.80^{+0.07}_{-0.06}$	81^{+2}_{-2}	$0.344^{+0.006}_{-0.006}$	$19.40^{+0.01}_{-0.01}$	1.09 (544)
	D1	$2.59^{+0.07}_{-0.07}$	71^{+2}_{-2}	$0.362^{+0.007}_{-0.007}$	$18.55^{+0.01}_{-0.01}$	1.13 (519)
	D2	$2.52^{+0.07}_{-0.06}$	65^{+2}_{-2}	$0.358^{+0.007}_{-0.007}$	$17.53^{+0.01}_{-0.01}$	1.17 (495)
	D3	$2.45^{+0.06}_{-0.06}$	63^{+2}_{-1}	$0.342^{+0.006}_{-0.006}$	$17.16^{+0.01}_{-0.01}$	1.12 (509)
	D4	$2.46^{+0.06}_{-0.06}$	63^{+2}_{-1}	$0.323^{+0.006}_{-0.006}$	$16.80^{+0.01}_{-0.01}$	1.12 (509)

FS is the flare segment.

peak abundance (Z) and the peak X-ray luminosity (L_{XF}) of flares were found to be 0.25, 0.299, and 0.362 $Z_\odot$ and $10^{31.21}$, $10^{31.23}$, and $10^{32.29}$ erg s^{-1} for the flare F1, F2, and F3, respectively. We found that temperature peaked either earlier than the emission measure or simultaneously with the emission measure. The abundance peaked after the emission measure for flares F1 and F3, whereas for flare F2, it peaked with the emission measure and remained constant thereafter for the initial phase of the flare decay.

4.3.3 Loop Modeling

To determine the loop length from the decay phase of the flares using the hydrodynamic loop model, we used equation 3.4 as mentioned in Chapter 3. Fig. 4.4 shows $\log(\sqrt{(EM)})$

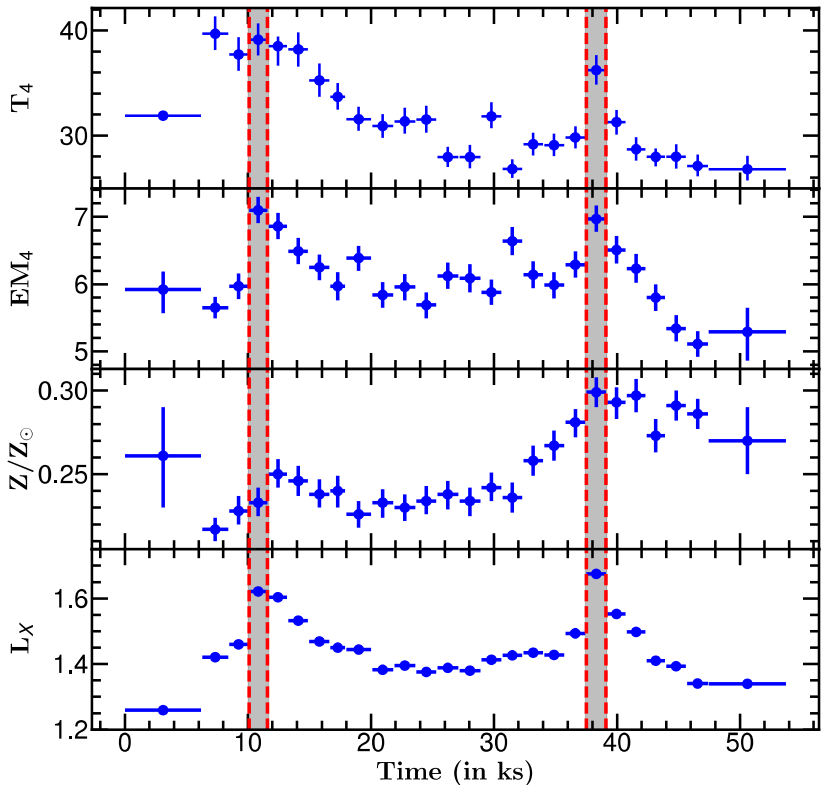

(a) A1

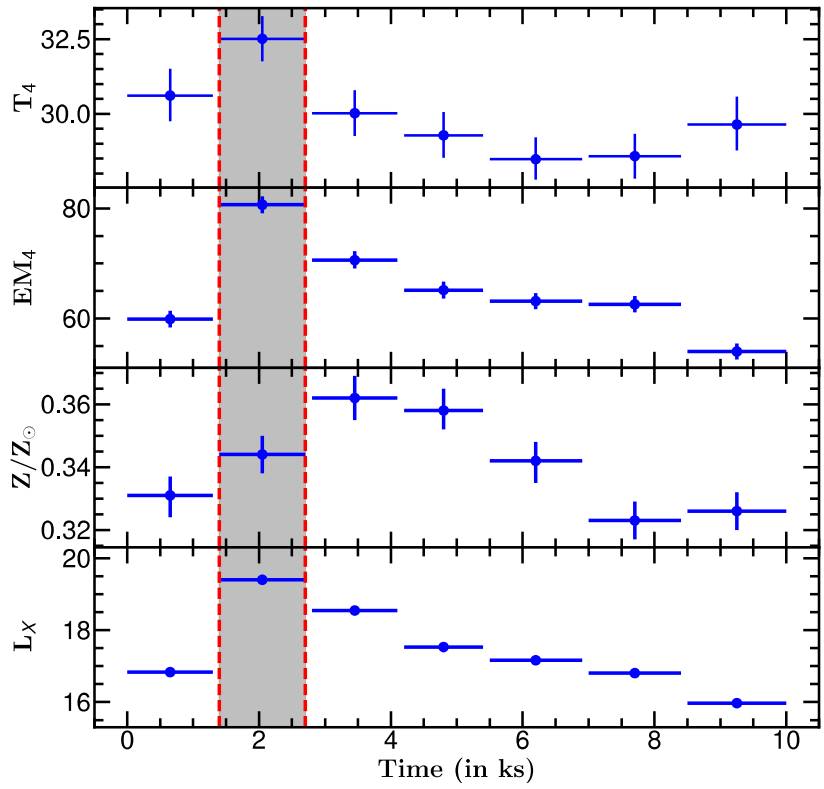

(b) A2

Figure 4.3: The temporal variation of spectral parameters T_4, EM_4, Z, and Luminosity L_{XF} for sets A1 and A2. The T_4 is in units of MK, EM_4 in 10^{53} cm^{-3}, L_{XF} in 10^{31} erg/s. The shaded regions show the peak phase of the corresponding flare.

vs. log(T) diagram (equivalent to the density vs temperature diagram) for all three flares, along with the best-fit straight line and corresponding ζ values. The value of ζ in the range of 0.36 to 1.6 suggests sustained heating during the flare's slow decay phase (see Reale, 2007, for detail). For flare F1 and F2, the value of ζ is above the critical value but well with a 1σ level, whereas for flare F3, ζ was found to be 1.03 ± 0.07. These values indicate the non-negligible heating during the decay phase of the observed flares.

The T_0 is the maximum best-fit segmented average temperature derived from the spectral fitting in units of K, whereas (T_{max}) is the maximum temperature of the flare calculated using the equation 3.5. The T_{max} for the flare F1, F2, and F3 were found to be 84±3, 76±3, and 67±2 MK, respectively.

The derived loop lengths were found to be in the range $5.9 - 8.9 \times 10^{10}$ cm as given in Table 4.4. Assuming a single cylindrical loop with half loop length L, we have derived some more physical parameters like loop volume (V), plasma density (n_e), plasma pressure at loop apex (P), the minimum magnetic field required to confine the plasma inside the flaring loop (B_{min}), total magnetic field (B_{Total}), heating rate (E_{HR}), and the total energy related to the heating rate ($E_{H,Total}$). Didel et al. (2024) have also performed such estimations for the corona of AB Dor. All these parameters are mentioned in Table 4.4.

4.4 Discussion and Conclusions

Our study of the active RS CVn binary HR 1099 provides a detailed analysis of the three energetic X-ray flares. The duration of these flares is found in the range of 2.8 to 4.1 h. The flare duration of these three flares is in between the flare duration observed in other flares in HR 1099, which were in the range of 1 to 9 hr (Audard et al., 2001; Nordon and Behar, 2007; Osten et al., 2004; Pandey and Singh, 2012). However, these flares are of very short duration in comparison to the longest duration flares observed in HR 1099 on

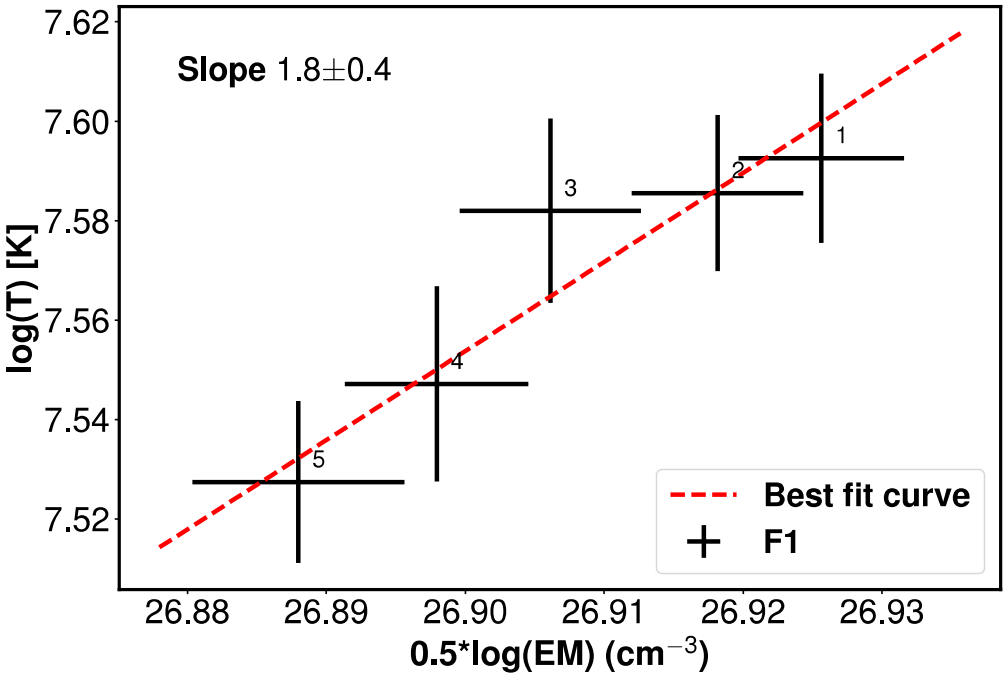

(a) F1

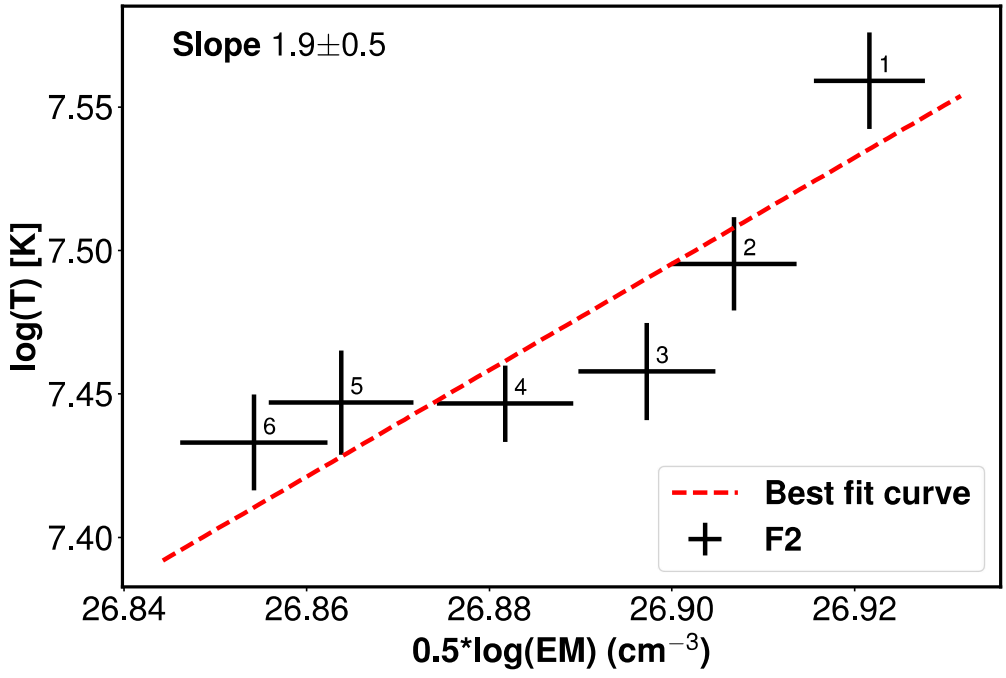

(b) F2

Figure 4.4: The density vs temperature (n-T) plot, where $EM^{1/2}$ is considered as the proxy of density. ζ is the slope of the n-T diagram from the decay phase of the flares (a) F1, (b) F2, and (c) F3.

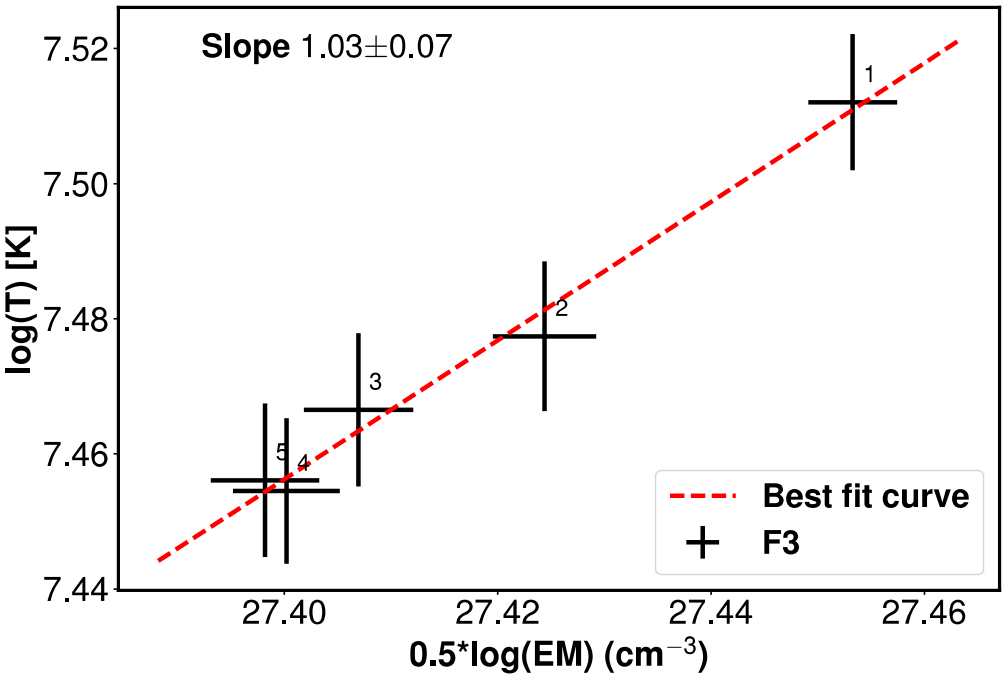

(c) F3

Figure 4.4: Continued...

Table 4.4: Loop parameters.

Flare (→) Parameters (↓)	F1	F2	F3
L_{XF} (10^{31} erg s^{-1})	10.55 ± 0.03	11.79 ± 0.03	106.3 ± 0.2
$E_{X,Total}$ (10^{35} erg)	6.8 ± 0.3	8.1 ± 0.5	107 ± 4
T_0 (MK)	39 ± 1	36 ± 1	32.5 ± 0.8
T_{max} (MK)	84 ± 3	76 ± 3	67 ± 2
L (10^{10} cm)	> 6.0	>5.9	8.9 ± 0.5
h/R_*	>0.14	>0.14	0.21±0.01
V (10^{31} cm^3)	>1.36	>1.29	4.4±0.8
n_e (10^{11} cm^{-3})	<2.5	<2.6	4.8±0.4
P (10^3 dyne cm^{-2})	<5.3	<4.9	8.0±0.7
B_{min} (G)	<364	<351	448±20
B_{Total} (G)	~608	~558	530±28
E_{HR} (10^{31} erg s^{-1})	~2.0	~1.4	1.4±0.2
$E_{H,Total}$ (10^{35} erg)	~1.3	~1.0	1.4±2
M_{CME} (10^{19} g)	~3.04	~3.25	~14.5

Note. Here, loop height, h = 2L/π and R_* is the radius of the star.

two different occasions, with a flare duration of >2.3 and ~ 2.8 days, respectively (Feldman and Laming, 2000; Karmakar, 2024).

Our analysis further explores the e-folding rise and decay times of these flares, revealing the rise time ranging from 10 to 38 minutes and decay time from 1.25 to 2.4 h. This pattern of a rapid rise followed by a more gradual decay aligns with established characteristics observed in other stellar flares from HR 1099 and similar RS CVn systems. For instance, previous studies have reported a rise time between 18 and 84 minutes and a decay time from 0.8 to 1.9 h (Pandey and Singh, 2012; Yan et al., 2021). Moreover, Osten et al. (2004) found the rise and decay times of the X-ray flares from HR 1099 in the range of 1.4 - 11.1 h and 2.6 - 13.2 h, respectively, for the observations from ASCA (0.6 - 10 keV), RXTE (2 - 12 keV), and BeppoSAX (0.6 - 10 keV). Further, Mullan et al. (2006) and Tsuboi et al. (2016) reported even longer decay times, ranging from 1.6 to 6.6 h with EUVE (7-76 nm) and 1.7 to 18.6 h with MAXI/GSC (2-30 keV), respectively. Additionally, the peak flare to quiescent state count rate ratio (A_P/A_Q) was found to be 1.2 for flares F1 and F2 and 1.4 for flare F3, which is the typical range for the energetic flares in the active stars (Didel et al., 2024; Pandey and Singh, 2008, 2012).

We have also estimated the flare frequency based on observations from 1978 to 2024. During a total observing time of 142 days, 57 flares were detected, leading to an estimated flare frequency of 0.4 flares per day. This translates to approximately one flare per rotation period of HR 1099. While the flare frequency in HR 1099 is lower than that of the highly active ultra-fast rotator AB Dor (Singh and Pandey, 2024), it significantly exceeds the occurrence rate of X-class flares observed on the Sun. However, due to the limited dataset and small sample size for HR 1099, we were unable to plot the flare frequency distribution function as shown in Figure 10 of Althukair and Tsiklauri (2023a). They found a power-law index (α) of 2.0±0.2 for K-type dwarfs, following the relation dN/dE $\propto E^{-\alpha}$. Future

research will expand this study to include more K-type subgiants, enhancing statistical significance and deepening our understanding.

The quiescent state of HR 1099 is characterized by a four-temperature plasma, in which the coolest three temperatures represent the quiescent state of HR 1099 with values of 3.02, 6.96, and 12.53 MK and an average temperature of 9.4 MK. The presence of a fourth temperature during the pre-and post-flare state could be due to the presence of flaring components as both flares F1 and F2 are observed one after another. From high-resolution X-ray spectra, the three temperature quiescent state was modeled using VAPEC with temperatures 4.5, 9.6, 20.2 MK with a weighted average temperature of 15.1 MK and average EM of $2.6 \times 10^{53} cm^{-3}$; the average quiescent temperature and EM is found to be similar to the previous results with 4-T quiescent as reported by Audard et al. (2001, 2003) with values nearly 17 MK and 2-T quiescent by Osten et al. (2004) with values 18.6 MK and $4 \times 10^{53} cm^{-3}$. However, Bozzo et al. (2024) reported the 4-T quiescent with lower plasma parameters like the average temperature of 6 MK, whereas average EM of $1.3 \times 10^{52} cm^{-3}$.

The TRS of the flaring spectra provides detailed insights into the physical processes occurring within the flaring region and helps to understand the flare evolution. According to the general flare evolution scenario, a heat pulse causes a rapid increase in the temperature throughout the loop. This heat is conducted from the hot regions to the cooler chromosphere, causing the chromospheric plasma to expand upward and evaporate explosively. Once the evaporation rate slows down, it balances with cooling, and the plasma cools rapidly through conduction while its density increases. Eventually, radiative cooling becomes more effective than conduction, causing the density to peak and the loop to start to deplete. Radiative cooling then becomes the dominant cooling mechanism (Reale, 2007, 2014; Serio et al., 1991). The observed increment in coronal loop temperature, plasma density, and abundance resembles the plasma heating and chromospheric evaporation scenario in

the observed flaring loops. Meanwhile, during the decay phase of the flare, the decrease in these parameters indicates the cooling mechanism with sustained heating. However, in the present case, due to the limited time resolution, we could observe that the temperature peaked either during the rising phase or simultaneously peaked with the luminosity and emission measure or at the peak phase of the flares. However, the abundances peaked after the emission measure peak, which is evidence of chromospheric evaporation.

The TRS results show averaged peak temperatures of 39.44, 35.96, and 32.48 MK, emission measures of 7, 7, and 81×10^{53} cm^{-3} for flares F1, F2, and F3, respectively. Further, we found the global abundances of 0.250, 0.299, and 0.362 $Z_{\odot}$, peak X-ray luminosities (L_{XF}) of 1.62, 1.68, and 19.40×10^{31} erg s^{-1}, and total flare energy of 6.8×10^{35}, 8.1×10^{35}, and 1.07×10^{37} erg. These results show similarity with the past results for this active star observed with various instruments like EUVE, MAXI, Chandra, Swift, etc. (Karmakar, 2024; Mullan et al., 2006; Nordon and Behar, 2007; Tsuboi et al., 2016). Veronig et al. (2002), Christe et al. (2008), and Tsuboi et al. (2016) established a relationship between flare duration and total flare luminosity, expressed as $\tau \propto L_{XF}^{\alpha}$, where α represents the slope of the log-log plot of flare duration (τ) versus luminosity (L_{XF}). Based on data from the Sun and nearby stars, they reported slopes of approximately 0.33, 0.2, and 0.2±0.03 for energy ranges of 3.1-24.8 keV, 6-12 keV, and 0.1-100 keV, respectively. Additionally, Maehara et al. (2015) and Althukair and Tsiklauri (2023b) reported a similar relationship using optical data from the KEPLER mission. Using our limited data sample, we obtained a slope of 0.18±0.01 in the energy range of 0.3-10.0 keV, as shown in Fig. 4.5.

We derived the semi-loop lengths of the flares using the hydrodynamic loop model, finding them to range between 5.9 and 8.9 $\times 10^{10}$ cm. In comparison, typical loop lengths for solar flares are of the order of 10^9 - 10^{10} cm. The loop heights (h = $2L/\pi$) corresponding to these semi-loop lengths constitute a small fraction of the radius of HR 1099. The h/R_* ratios for these flares were found to be 0.14 for both F1 and F2 and 0.21 for the flare F3.

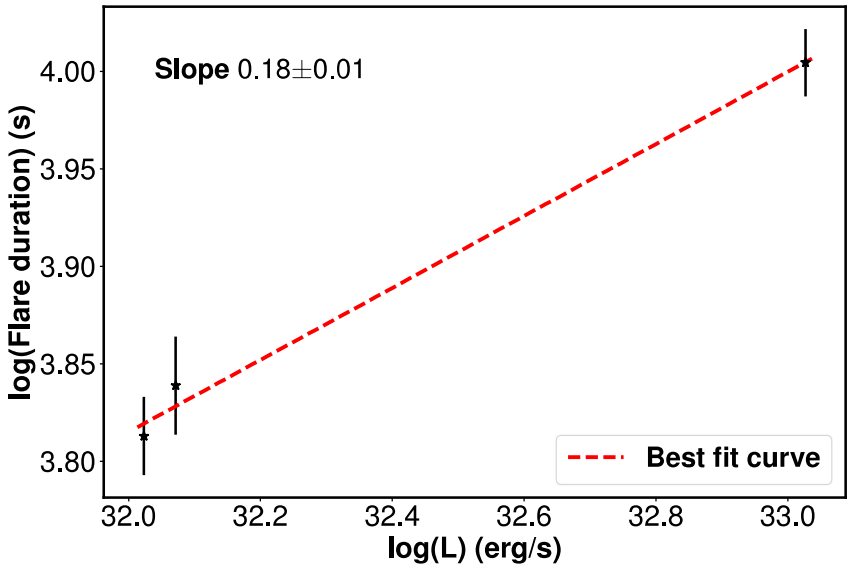

Figure 4.5: Log-log plot of flare duration versus luminosity with linear curve fit.

Mullan et al. (2006) reported the value of L and the ratio h/R_* in the range of 4.8-12.7 $\times 10^{10}$ cm and 0.1 to 0.3 for HR 1099.

The total X-ray energy released during the flares was estimated to be between 6.8 $\times$ 10^{35} and 10.7 $\times$ 10^{36} erg, which is substantially higher than the total energy of the most powerful solar flares (Emslie et al., 2012; Zimovets et al., 2020). The calculated loop volume V, electron density n_e, and plasma pressure P were found to be in the range of 1.3 - 4.4 $\times$ $10^{31} cm^3$, 2.5 - 4.8 $\times$ $10^{11} cm^{-3}$, and 5 - 8 $\times$ 10^3 dyne cm^{-2}. Additionally, the total magnetic field strength B_{Total} of the loops was found to be between 500 to 600 G, similar to typical magnetic field observations for HR 1099 (Mullan et al., 2006; Pandey and Singh, 2012) and the minimum magnetic field B_{min} in the range of 350 - 448 G (110-320 G; Mullan et al., 2006).

The mass of ejected CME associated with the flare can be estimated with the relation $M_{CME}(g) = 10^{-1.5\pm0.5} E_G^{0.59\pm0.02}$, where E_G is the energy released during the flare in GOES (1 – 8 Å) energy band (Aarnio et al., 2012; Drake et al., 2013), which can be converted from XMM-Newton flux from 0.3-10.0 keV band to GOES flux using WEBPIMMS. The M_{CME} for HR 1099 was found to be in the range of approximately 3.0 - 14.5 $\times$ 10^{19} g,

which was found to be maximum for flare F3 as mentioned in Table 4.4. These values are approximately 100 to 1000 times higher than the most massive solar CME reported (Yashiro and Gopalswamy, 2009). However, they exceed the mass of CMEs observed on other active stars such as AB Dor, EQ Peg, EK Dra, etc., which have typical CME masses in the range of 10^{18-19} g (Didel et al., 2024; Karmakar et al., 2022; Namekata et al., 2021). Based on the calculated parameters for HR 1099 using X-ray data, such as flare temperature, emission measure, loop length, magnetic field, etc., it is evident that the study of flare parameters plays a crucial role in understanding the coronal dynamics of the magnetically active stars. The more resolved data and multi-wavelength perspective can provide a comprehensive understanding of the geometry of the corona and the physical processes happening during these flares in detail.